RSC Advances

PAPER

View Article Online
View Journal | View Issue

Cite this: *RSC Adv.*, 2026, **16**, 4335

Exploration of the interaction strength at the interface of neutral chalcogen ligands and gold surfaces

Talia Alexandra Garzón,[a] Mary Tabut,[bc] Monica Calatayud,[b] Fernando Mendizabal *[d] and María Luisa Cerón *[a]

Using dispersion-corrected density functional theory (DFT-D3), this study systematically examines the adsorption behavior of Au(XR) species (X = S, Se, Te; R = –H, $–CH_3$, $–C_6H_{11}$) on gold surfaces of different morphologies Au(111), Au(100), Au(110), Au(321), and Au(32$\bar{1}$). The results demonstrate that the interaction strength increases with both the chalcogen's polarizability and the steric size of the substituent (Te > Se > S and –H < $–CH_3$ < $–C_6H_{11}$). A clear relationship between surface reactivity and dispersion contribution is established: while Au(111) adsorption is governed by long-range van der Waals interactions, rougher surfaces such as Au(110) and Au(321) promote stronger chemisorption through bridge-type bonding. Notably, a dispersion threshold of approximately 45% distinguishes between physisorbed and chemisorbed regimes. Bader charge and PDOS analysis further reveals charge transfer from the metal slab to the ligand, increasing from S to Te. These findings offer a comprehensive structure–energy relationship that can guide the rational engineering of chalcogen–gold interfaces with tailored electronic and structural properties.

Received 23rd October 2025
Accepted 27th December 2025

DOI: 10.1039/d5ra08118a

rsc.li/rsc-advances

1. Introduction

Surface property modification of metallic substrates has garnered significant attention for its wide-ranging applications in nanotechnology,[1] as well as in areas such as adhesion, friction,[2–4] protection,[5] corrosion resistance,[6] catalysis,[7] and wettability.[8] In synthetic nanotechnology, precise control over the morphology and surface termination of metal nanoparticles (NPs) is critical, as their shape is closely tied to their activity and functional properties.[2–4] Over the past few decades, considerable progress has been made in shaping gold nanoparticles (AuNPs),[5–7] which has expanded their utility in key areas such as sensing,[7] biomedicine,[1,9] chirality,[10,11] and catalysis.[12,13]

One of the most effective strategies for modifying surface properties is using self-assembled monolayers (SAMs).[9–15] These are semi-rigid, two-dimensional layers formed by molecules that covalently bind to a substrate, imparting new chemical characteristics to the surface.[16–21] SAM-forming molecules typically consist of three essential components: a head group that binds firmly to the substrate, a terminal group that defines the external surface chemistry, and a spacer (which can be an aliphatic chain, aromatic group, or mixed structure) separating the head and terminal groups.[22–24]

Traditionally, SAMs have utilized thiols (–SH) as the head group to anchor molecules to noble metals, particularly gold surfaces,[22–24] due to their ease of preparation and stability.[6,25–27] However, alternatives to sulfur (S) as the anchor atom are being explored,[28,29] with selenium (Se) and tellurium (Te), other elements from the chalcogen group, emerging as promising candidates.[30,31] Theoretical studies on ligand interactions with gold substrates containing chalcogens have revealed that these interactions are primarily driven by electrostatic forces, with a smaller but significant contribution from dispersive interactions.[30] Nevertheless, studies on extended systems incorporating dispersion effects on heavier chalcogen elements interacting with gold surfaces remain limited.[31,32] These advanced approaches are essential for deepening our understanding of the properties and stability of interactions between ligands and metallic substrates, particularly through the identification of the intra and intermolecular interactions between ligands and gold atoms.

In this work, the nature of molecular bonding in complex inorganic systems is examined, with particular emphasis on how structural variations, gold surface morphology, and electronic dispersion effects influence the interaction with chalcogen-based neutral ligands (Au(XR), where X = S, Se, Te; and R = $–H_2$, $–CH_3$, $–C_6H_{11}$). To account for both

[a]*Facultad de Ingeniería, Universidad Finis Terrae, Av. Pedro de Valdivia 1509, Providencia, Santiago, Chile. E-mail: lceron@uft.cl*

[b]*Sorbonne Université, CNRS, MONARIS, CNRS-UMR 8233, 4 Place Jussieu, F-75005 Paris, France*

[c]*Sorbonne Universite, CNRS, Laboratoire de Chimie Théorique, LCT, 4 Place Jussieu, F-75005 Paris, France*

[d]*Departamento de Química, Facultad de Ciencias, Universidad de Chile, Casilla 653, Santiago, Chile. E-mail: hagua@uchile.cl*

thermodynamic stability and the potential for enantioselective interactions, five representative Au surfaces (111), (100), (110), (321), and (32$\bar{1}$) are considered, following the approach reported by Morales-Vidal *et al.*[33] in their study of amino acid adsorption, see Fig. 1. This selection enables a systematic comparison between achiral low-Miller-index facets and high-index chiral terminations, thereby providing a comprehensive framework to evaluate the role of chalcogen atoms and dispersion forces in modulating surface reactivity. In this work, we restrict our analysis to molecular adsorption modes of XR on Au(*hkl*) surfaces. Dissociative pathways or reaction intermediates are beyond the scope of the present study, as our objective is to evaluate comparative interaction strengths and geometric/electronic trends.

2. Computational details

The Perdew–Burke–Ernzerhof (PBE) exchange-correlation functional[34] was employed, along with van der Waals corrections[35] using the Grimme D3 method,[36] in all calculations performed with VASP version 6.2.1.[37–39] Core electrons were treated using projector-augmented wave (PAW) pseudopotentials.[40,41] For Au, H, and C atoms, 11, 1, and 4 valence electrons were used, respectively, while six valence electrons were assigned to the chalcogens (S, Se, and Te). A plane-wave basis set with a 450 eV cutoff[42] was applied in all cases. Structural optimizations were carried out using the Davidson algorithm (ALGO = FAST), with a maximum of 400 ionic steps and an energy convergence threshold of 1×10^{-6} eV. However, in some cases, for single-point energy calculations, the full diagonalization (ALGO = All) was required to ensure convergence of all electronic states.

Different morphologies of the gold substrate were utilized in this work to determine the orientations of the ligands on Au surfaces, as displayed in Fig. 1. Periodic boundary conditions were employed to model gold (Au) surfaces across three low-Miller-index planes (111), (110), and (100), as well as two high-Miller-index planes (321) and (32$\bar{1}$). The (111) and (110) surfaces were modeled using four atomic layers, whereas the (100) surface was constructed with eight atomic layers. For the (321) and (32$\bar{1}$) terminations, sixteen atomic layers were utilized. The number of layers for each surface was determined according to its degree of openness.[43] In all cases, the bottom half of the layers were kept fixed to replicate bulk behavior, while the top half was fully relaxed. A 15 Å vacuum region was incorporated between the slabs, accompanied by a dipole correction along the *z*-axis.[44] The models used are illustrated in Fig. 1 and were developed following a methodology like that described in the studies by Morales-Vidal *et al.*[33]

The studied Au surface was represented using different models: the Au(111) and Au(100) surfaces were described with p(4 × 4) slabs; the Au(110) surface was modeled with a p(3 × 3) slab; and the Au(321) and Au(32$\bar{1}$) surfaces were represented with p(2 × 2) slabs. The Brillouin zone for all models was sampled using a 3 × 3 × 1 *k*-point mesh generated using the Monkhorst–Pack method.[45] A single chalcogen molecule per unit cell was included to model a low-coverage system. All atomic structures and charge distributions were visualized using VESTA (Visualization for Electronic and Structural Analysis) software, version 3.90.0a.[46] In this study, the interaction energy (with and without dispersion corrections), the dispersion contribution percentage are presented in Table 1 and the gold complexes' charge in Table 2.

3. Models

3.1 Clean surfaces

For the development of this study, it is essential to conduct a preliminary analysis of the surface energy of the systems under consideration. In this work, the Au(100), Au(110), and Au(111) surfaces have been selected, as they are achiral. Additionally, the Au(321) and Au(32$\bar{1}$) surfaces are reported as chiral,[33,47] where Au(321) can be assigned the R configuration, while Au(32$\bar{1}$) corresponds to the S configuration.

These structural configurations are depicted in Fig. 1 and 2, with the latter providing a view along the *Z* direction, highlighting the surface topology where the ligands are adsorbed. To confirm the convergence of the total energy, eqn (1) was used to calculate the surface formation energy (γ in J m^{-2}) for the slab models. The expression for eqn (1) is as follows:[48]

$$\gamma = \frac{E_{\text{slab}} - nE_{\text{bulk}}}{2A} \quad (1)$$

where E_{bulk} represents the total energy of the bulk of gold per unit formula, and E_{slab} corresponds to the energy of the slab used in the models. The number of layers varies depending on

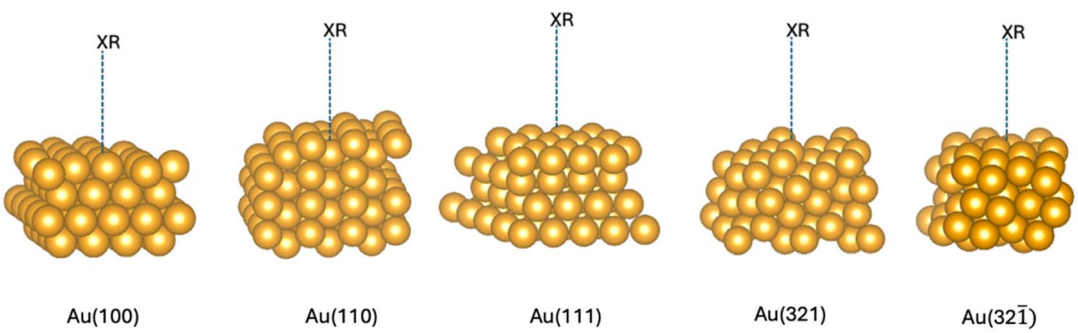

Fig. 1 Schematic view of the Au(XR) complexes (X = S, Se, Te, and R = $-H_2$, $-CH_3$, or $-C_6H_{11}$).

Table 1 Interaction energies between gold surfaces and XR (chalcogen compounds), where X = S, Se, Te and R = –H, $-CH_3$, $-C_6H_{11}$. Energies listed correspond to the total interaction energies ΔE_{int}(PBE-D3) and without the dispersion contribution ΔE_{int}(PBE). The percentage of dispersion term is included. All energies are in eV

	ΔE_{int} PBE-D3			ΔE_{int} PBE			% Dispersion		
Au(*hkl*)–XR	S	Se	Te	S	Se	Te	S	Se	Te
Au100-XH_2	−0.630	−0.776	−1.064	−0.469	−0.540	−0.540	25.6	30.5	49.3
Au110-XH_2	−0.980	−1.142	−1.312	−0.710	−0.782	−0.782	27.6	31.5	40.4
Au111-XH_2	−0.561	−0.708	−0.969	−0.159	−0.216	−0.216	71.6	69.4	77.7
Au321-XH_2	−0.869	−1.075	−1.242	−0.552	−0.607	−0.607	36.5	43.5	51.2
Au32-1-XH_2	−0.985	−1.194	−1.184	−0.614	−0.691	−0.691	37.7	42.1	41.6
Au100-$XHCH_3$	−0.939	−1.096	−1.373	−0.609	−0.681	−0.872	35.2	37.9	36.5
Au110-$XHCH_3$	−1.222	−1.376	−1.825	−0.895	−0.939	−1.310	26.7	31.8	28.2
Au111-$XHCH_3$	−0.855	−1.019	−1.285	−0.285	−0.374	−0.530	66.6	63.3	58.8
Au321-$XHCH_3$	−1.226	−1.665	−1.592	−0.780	−1.228	−0.972	36.4	26.3	38.9
Au32-1-$XHCH_3$	−1.189	−1.456	−1.556	−0.782	−0.877	−1.022	34.3	39.8	34.3
Au100-XHC_6H_{11}	−1.408	−1.557	−1.884	−0.534	−0.605	−0.838	62.1	61.1	55.5
Au110-XHC_6H_{11}	−1.558	−1.676	−1.979	−0.693	−0.749	−1.046	55.5	55.3	47.1
Au111-XHC_6H_{11}	−1.271	−1.454	−1.788	−0.159	−0.270	−0.465	87.5	81.5	74.0
Au321-XHC_6H_{11}	−1.689	−1.827	−2.126	−0.613	−0.705	−0.924	63.7	61.4	56.6
Au32-1-XHC_6H_{11}	−1.688	−1.793	−2.060	−0.671	−0.718	−0.911	60.3	60.0	55.8

the surface: four for Au(100) and Au(111), three for Au(110), and two for Au(321) and Au(32$\bar{1}$) systems. A is the area of the unit cell, and the factor 2 comes from the fact that each slab has two surfaces.[42] The choice of these numbers of layers ensures that the slab is thick enough to accurately represent both surface and bulk properties.

The calculated surface energies for all systems are shown in Fig. 2. It can be observed that for the achiral systems Au(100), Au(110), and Au(111), the energies are 1.55 J m^{-2}, 1.63 J m^{-2}, and 1.43 J m^{-2}, respectively. This indicates a trend of increasing energy: Au(110) > Au(100) > Au(111), a trend that has also been observed in other studies with values similar to those obtained in this study.[49–51] In contrast, for the chiral systems Au(321) and Au(32$\bar{1}$), the energy remains at 1.59 J m^2, which is the value reported by Morales-Vidal *et al.*[33] These values are relatively close to the experimental value for the surface of Au(111), which is 1.50 J m^{-2}.[52,53]

3.2 Models for chalcogen ligands and gold surfaces

As mentioned in the Computational details, to study the dispersion effects generated by chalcogens on gold surfaces under low coverage conditions, Au(XR) type systems are modeled, where X represents the chalcogen element (S, Se, Te) and R corresponds to three types of substituents: –H, $-CH_3$ and $-C_6H_{11}$. In all cases, the neutral state of the system is maintained by adding a hydrogen atom bonded to the chalcogen, which electronically stabilizes the adsorbed species.

Fig. 3 illustrates the models presented in this study schematically, the gold surfaces are represented by blocks on which the different XR species adsorb. In each case, different initial orientations of the molecule with respect to the surface were considered, including horizontal (Fig. 3a, c, and e) and vertical (Fig. 3b, d, and f) geometries, to represent the possible adsorption configurations under low coverage conditions.

In all systems, the chalcogen atom is initially placed at the top site of the gold atom on the surface. It is fully relaxed to obtain the optimized configuration, as previously described, using DFT calculations to determine their minimum energy geometries. From these optimized structures, the adsorption energies were calculated with and without dispersion correction, along with the percentage of dispersive contribution; all these results are reported in Table 1. This strategy enables

Table 2 Bader charges (in |e|) of chalcogen molecules adsorbed on various Au(*hkl*) surfaces. Total bader charges are given for each molecule (XH_2, $XHCH_3$, XHC_6H_{11} with X = S, Se, Te) on Au(100), Au(110), Au(111), Au(321), and Au(32$\bar{1}$) surfaces. Values in parentheses correspond to the bader charge of the chalcogen atom (S, Se and Te)

	(100)	(110)	(111)	(321)	(32−1)
SH_2	−0.190 (−0.084)	−0.198 (−0.022)	−0.167 (−0.026)	−0.231 (−0.062)	−0.206 (0.013)
SeH_2	−0.252 (−0.271)	−0.243 (−0.226)	−0.221 (−0.274)	−0.274 (−0.304)	−0.234 (−0.209)
TeH_2	−0.362 (−0.647)	−0.361 (−0.665)	−0.351 (−0.631)	−0.387 (−0.669)	−0.386 (−0.659)
$SHCH_3$	−0.227 (−0.093)	−0.240 (−0.062)	−0.205 (−0.101)	−0.257 (−0.104)	−0.254 (−0.107)
$SeHCH_3$	−0.275 (−0.282)	−0.289 (−0.308)	−0.269 (−0.317)	−0.317 (−0.331)	−0.270 (−0.238)
$TeHCH_3$	−0.396 (−0.675)	−0.351 (−0.536)	−0.400 (−0.676)	−0.415 (−0.692)	−0.427 (−0.711)
SHC_6H_{11}	−0.235 (−0.039)	−0.253 (−0.064)	−0.214 (0.011)	−0.249 (−0.048)	−0.256 (−0.086)
$SeHC_6H_{11}$	−0.293 (−0.257)	−0.292 (−0.266)	−0.277 (−0.263)	−0.316 (−0.274)	−0.314 (−0.312)
$TeHC_6H_{11}$	−0.404 (−0.610)	−0.418 (−0.643)	−0.396 (−0.624)	−0.426 (−0.622)	−0.428 (−0.657)

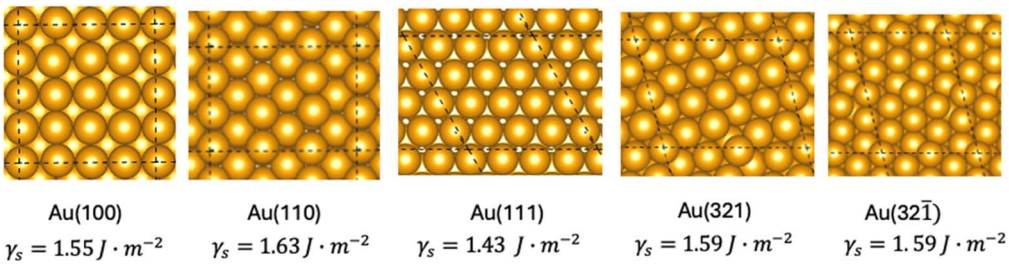

Fig. 2 Top view of gold surfaces considered in this study and their corresponding computed surface energies in J m^{-2}.

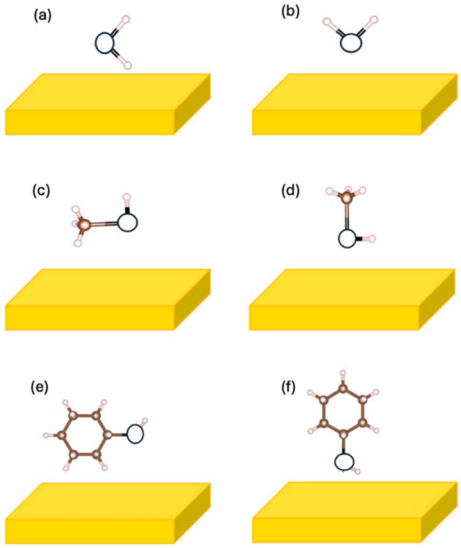

Fig. 3 Schematic representations of the XR species adsorbed on different gold surfaces: Au(100), Au(110), Au(111), Au(321), and Au(32$\bar{1}$), depicted as gold blocks. Panels (a), (c), and (e) correspond to horizontal molecular orientations, while (b), (d), and (f) show vertical configurations. Legend: (S, Se, or Te) = white sphere with blue circle; brown = carbon; white = hydrogen.

a systematic evaluation of how molecular orientation and the nature of the R group affect the stability and electronic properties of the interaction between the chalcogen and the gold surface.

4. Results and discussion

4.1 Interaction strength analysis

The interaction energies E_{int} between the chalcogens and the various gold surfaces are calculated using the following expression:[33,42]

$$E_{int} = E_{Au(hkl)-XR} - (E_{Au(hkl)} + n \cdot E_{XR}) \quad (2)$$

where $E_{Au(hkl)-XR}$ represents the total energy of the chalcogen-containing compound (where X = S, Se, Te and R = –H, $–CH_3$, $–C_6H_{11}$), $E_{Au(hkl)}$ corresponds to the energy of the gold surface, and E_{XR} is the energy of the isolated molecule. In this work, n = 1 since the calculations are performed under low coverage conditions with only one molecule. As mentioned above in Fig. 3, both vertical and horizontal geometries were considered for the molecules without dissociating the X–R bond, and the most stable configuration was selected based on its lower electronic energy.

Table 1 presents the results of the evaluation of eqn (2), which includes the energies of all systems studied at the PBE level, both with and without Grimme's correction. The dispersion percentages associated with each chalcogen on the different gold surfaces are also reported. The E_{int} values for all systems indicate that the inclusion of the dispersion correction results in more negative interaction energies (ΔE_{int}), confirming that this term is helpful in accurately describing adsorption. The magnitude of ΔE_{int} depends on the nature of the chalcogen (X = S, Se, Te) and on the substituent R, consistent with variations in polarizability and molecular size. The affinity for gold follows Te > Se > S, reflecting the higher polarizability of Te and its greater ability to establish stronger interactions with the surface. This pattern is consistent across the three XR ligand families and becomes more pronounced as the group progresses. The effect of R is likewise marked: on average, the interaction energy becomes more negative in the order XH_2 < $XHCH_3$ < XHC_6H_{11}, indicating that bulkier substituents promote adsorption. Stability also depends on the surface facet. For XH_2, the weakest interaction corresponds to Au(111)-SH_2 (−0.561 eV), whereas the strongest is observed for Au(110)-TeH_2 (−1.312 eV). For $XHCH_3$, the least stable system is Au(111)-SCH_3 (−0.855 eV) and the most stable is Au(110)-$TeCH_3$ (−1.825 eV). Finally, for XHC_6H_{11}, the strongest interactions in the entire series are reached, with Au(321)-TeC_6H_{11} (−2.126 eV) being the most negative; in contrast, within this family, the least negative value appears for Au(111)-SC_6H_{11} (−1.271 eV).

With respect to the contribution of dispersion, exceptionally high percentages are observed for systems with a vertical geometry on the Au(111) surface, as discussed below. These results show that, beyond substituent size, the molecular orientation and the specific surface strongly condition the importance of dispersion forces in stabilizing the adsorbate-surface system. Additional tests performed with the r^{2}SCAN meta-GGA functional with rVV10[54] on a representative weakly bound system (SH_2/Au(111)) and a strongly interacting configuration (XC_6H_{11}/Au(321)) confirm that the relative energetic trends are preserved. Although r^{2}SCAN yields slightly more stabilizing adsorption energies, the stability order between flat and stepped Au surfaces remains unchanged, supporting the

robustness of the conclusions obtained with the original GGA + D3 approach (see Table S1 in SI)

4.2 Influence of surface morphology and dispersion

Fig. 4 shows the dispersion for the XR (X = S, Se, Te; R = H_2, HCH_3, HC_6H_{11}) on the five surfaces studied. Au(111) stands out with the highest values: for XHC_6H_{11} it reaches 87.5% (S), 81.5% (Se), and 74.0% (Te), and it is also high for XH_2 ($\approx$70–77%) and $XHCH_3$ ($\approx$58–66%). For a given surface, the dispersion fraction increases with substituent size ($XH_2 \rightarrow XHCH_3 \rightarrow XHC_6H_{11}$), suggesting that long-range van der Waals contacts become more important as the group becomes bulkier.

Fig. 4 also shows that the more reactive surfaces Au(321)/Au(32$\bar{1}$) and Au(110) exhibit lower dispersion percentages (*e.g.*, $XH_2 \approx$ 40–43%, $XHCH_3 \approx$ 25–40%, $XHC_6H_{11} \approx$ 55–62%) and, on average, display more negative ΔE_{int}, indicating a predominance of the chemical contribution to stabilization. This trend is consistent with their higher surface energies ($\gamma \approx 1.59$ J m^{-2} for Au(321)/Au(32$\bar{1}$) and $\gamma \approx 1.63$ J m^{-2} for Au(110)) compared with the compact Au(111) facet ($\gamma \approx 1.43$ J m^{-2}), where van der Waals interactions tend to dominate. Finally, Au(100) remains the least favorable facet, particularly for XH_2.

4.3 Structural and charge analysis

Before analyzing the bonding geometry in detail, it is important to assess whether adsorption induces any modification of the surface structure. A comparison between the clean and adsorbate-covered slabs (Fig. S1–S4) shows that adsorption produces only localized relaxation of the topmost Au layer. Vertical displacements remain within 0.05–0.20 Å, while in-plane Au–Au distances deviate by less than 2–3% from the clean surfaces. No lateral rearrangements, loss of periodicity, formation of adatoms, or step restructuring were observed. Therefore, the Au(*hkl*) terminations preserve their terrace-step morphology, indicating that XR adsorption leads to minor local relaxation rather than true surface reconstruction.

The preferred adsorption site for each surface was also determined from the most stable optimized geometries. On Au(32$\bar{1}$), XR species bind at the step-edge Au atom, maximizing interaction with under-coordinated sites. On Au(110), adsorption occurs at a bridge site between the Au rows along the [$\bar{1}$10] direction. On Au(321), the chalcogen atom preferentially occupies the step/kink region of the terrace step structure. These adsorption sites were consistently observed for all XH_2, $XHCH_3$ and XC_6H_{11} species.

Fig. 5 and 6 illustrate the optimized adsorption geometries of the Au(XR) systems, where X = S, Se, Te, and R = H_2, CH_3, C_6H_{11}, corresponding to the highest and lowest energy configurations, respectively. As shown in Fig. 5, the complexes with the highest interaction energies are located on the Au(111) surface, which represents the least reactive termination within the studied set. In these configurations, the ligands adopt

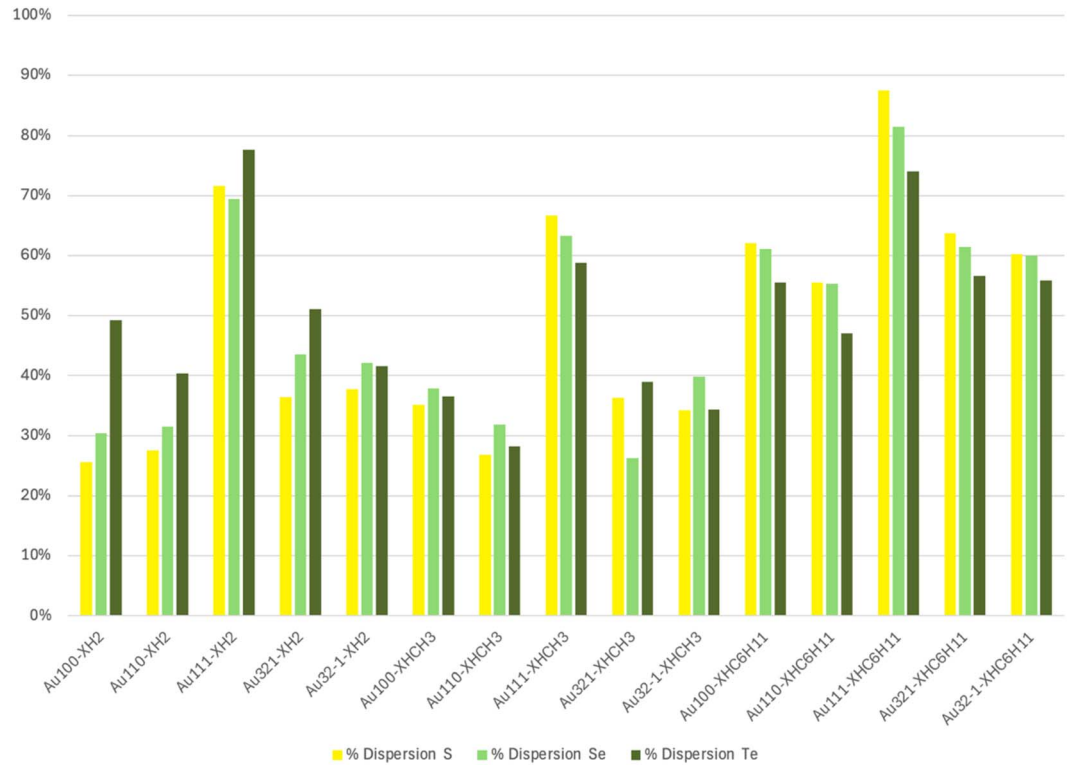

Fig. 4 Dispersion percentage in adsorbate–surface stabilization for XR (chalcogens compounds), where X = S, Se, Te and R = –H, $-CH_3$, $-C_6H_{11}$ on gold surfaces. Au(111) is dominated by van der Waals interactions (maxima for XHC_6H_{11}), whereas Au(321)/Au(32$\bar{1}$) and Au(110) (reactive surfaces) show a lower dispersion percentage and more negative ΔE_{int}, evidencing a greater chemical contribution. The trend $XH_2 < XHCH_3 < XHC_6H_{11}$ is also observed.

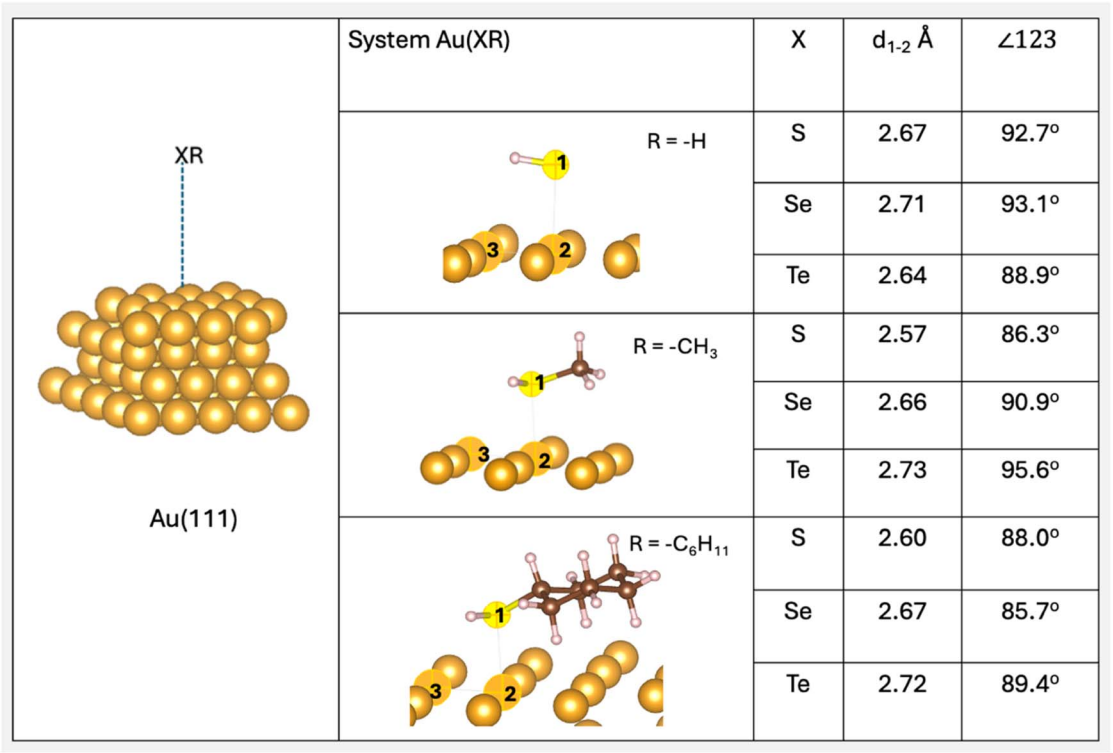

Fig. 5 Optimized adsorption geometries of Au(XR) species (X = S, Se, Te; R = –H, $-XCH_3$, $-XC_6H_{11}$) on the Au(111) surface, showing characteristic Au–X distances (d_{1-2}) and X–Au–Au angles (∠123). These configurations correspond to the systems with the highest interaction energy values (least stable adsorption) within the studied series.

nearly perpendicular orientations relative to the surface, with longer Au–X distances and larger X–Au–Au angles, consistent with weaker adsorption dominated by dispersive interactions. Conversely, Fig. 6 displays the most stable adsorption geometries, located on stepped and chiral surfaces Au(321), Au(32$\bar{1}$), and Au(110). These configurations exhibit shorter Au–X distances and smaller X–Au–Au angles, reflecting stronger chemisorptive interactions. The comparison between both figures highlights a clear correlation between surface morphology and adsorption strength: flat surfaces favor weak, dispersion-driven physisorption, whereas stepped terminations promote stronger chemical bonding and greater stabilization of the Au–X interaction. These parameters enable the correlation of geometry and stability, highlighting the strength of the interaction between the chalcogen (X = S, Se, Te) and the substituent R on the gold surfaces.

Furthermore, Fig. 5 and 6 show that increasing chalcogen polarizability (Te > Se > S) and substituent size (–H < $-CH_3$ < $-C_6H_{11}$) systematically drive ΔE_{int} toward more negative values, thereby enhancing the strength of the chalcogen–gold interaction. The series spans from the most stable Au(321)-$TeHC_6H_{11}$ to the least stable Au(111)-SH_2. On the other hand, it is acknowledged that surface thiols (SH) typically dehydrogenate on gold to yield thiolate species.[55,56] However, in this study, only non-dissociated X–H ligands are considered to enable a consistent comparison among neutral adsorbates. Consequently, the XH_2 cases appear less stabilized than would be expected for their deprotonated counterparts (X^-),[57] whose treatment is ionic by nature and falls outside the scope of the present work.

In addition, the gold surfaces modulate the geometry and stability: Au(111) tends to favor more vertical TOP-side orientations with a high dispersion contribution (see Fig. 5); while Au(321), Au(32$\bar{1}$) and Au(110) stabilize bridge configurations with stronger interactions (more negative ΔE_{int}), a lower percentage of dispersion (~20–40%), d_{1-2} < 2.6 Å, and angles of 50–70° (see Fig. 6). In contrast, the configurations predominantly on Au(111) (the most stable surface, as shown in Fig. 2 for clean surfaces), exhibit d_{1-2} > 2.6 Å, a higher dispersion contribution (~70–80%), TOP-side orientation, and angles of 85–95°. This is consistent with previous reports for chalcogens on Au(111), where the TOP-side configuration is preferred,[58–60] suggesting that neutral chalcogen species tend to stabilize in TOP-side positions on Au(111) due to the high stability of the Au(111) surface.

Table 2 presents the Bader charge analysis for the series of chalcogen-containing molecules (–H, $-CH_3$, and $-C_6H_{11}$, with X = S, Se, Te) adsorbed on each distinct gold crystallographic plane [(*hkl*)] considered in this work. In all cases, the total charge transfer from the surface to the molecule is negative, indicating a net transfer of electrons from the metal to the adsorbed molecule. The magnitude of charge transfer increases systematically from S to Te across all surface orientations, which can be attributed to the increasing polarizability and atomic size of the heavier chalcogens. The substitution of

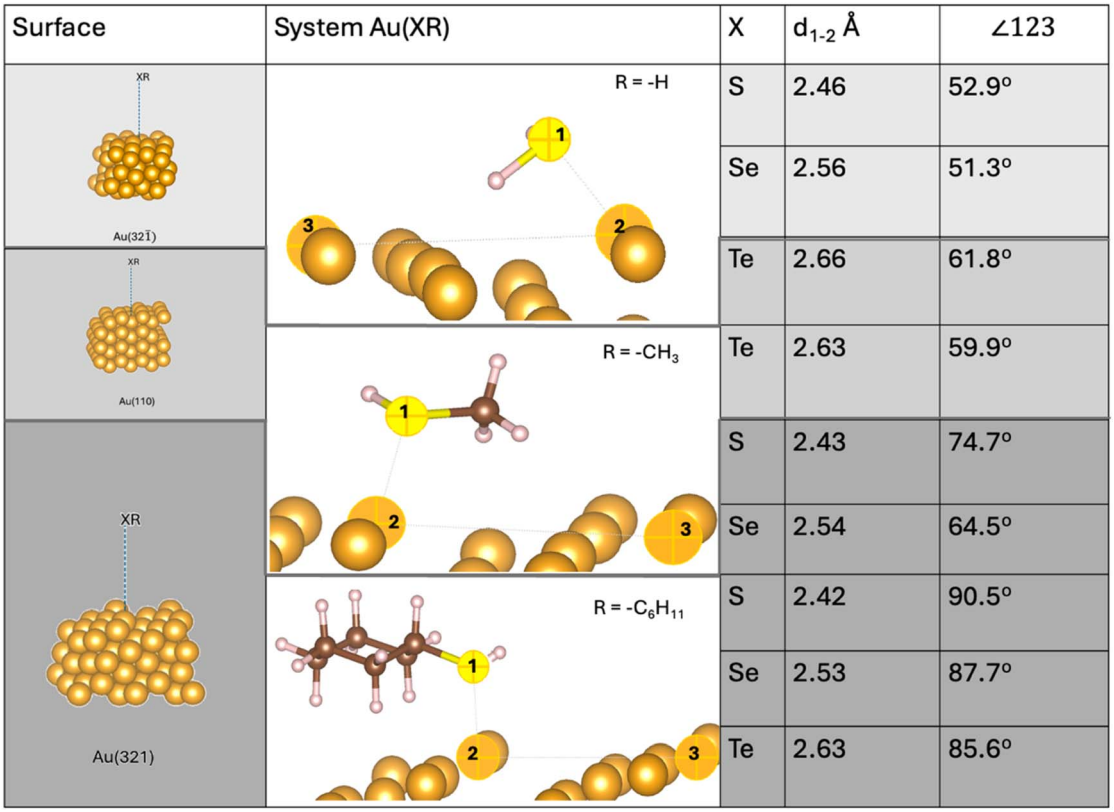

Fig. 6 Optimized adsorption geometries of Au(XR) species (X = S, Se, Te; R = $-H_2$, $-CH_3$, $-C_6H_{11}$) on stepped and chiral gold surfaces Au(32$\bar{1}$), Au(110), and Au(321), showing characteristic Au–X distances (d_{1-2}) and X–Au–Au angles (∠123). These configurations correspond to the systems with the lowest interaction energy values (most stable adsorption) within the studied series.

dihydrogen with electron-donating groups ($-CH_3$ or $-C_6H_{11}$) leads to a modest but systematic increase in charge transfer, especially for Se and Te derivatives, supporting the role of the nature of the anchoring atom in modulating surface interactions.

Interestingly, no direct correlation is observed between the magnitude of charge transfer (either total or on the chalcogen atom) and the calculated interaction energies. However, among the surfaces studied Au(111) consistently exhibits the lowest charge transfer and also corresponds to the least stable adsorption configurations, which is consistent with its relatively inert and closely packed nature. For the most stable systems (*i.e.* those with the strongest interaction energies), no clear dependence on the total molecular charge or the chalcogen charge can be established. This suggests that factors beyond simple charge accumulation, such as geometric orientation, orbital overlap or surface electronic structure, may play a more dominant role in dictating adsorption strength.

Notably, the chiral Au(321) and Au(32$\bar{1}$) surfaces consistently induce greater electron accumulation on the chalcogen atom compared to the achiral Au(100), Au(110), and Au(111) surfaces. This is consistent with the presence of low-coordination sites (*e.g.* steps and kinks) on the chiral facets, which enhance molecule–surface interactions. This trend aligns with the stronger interaction energies observed for most systems on these surfaces.

In terms of charge distribution, the chalcogen atom generally accommodates the majority of the transferred electron density. This trend is particularly pronounced for tellurium-containing species, with Bader charges as low as −0.711 |e| on the Au(32$\bar{1}$) surface for Te in $TeHCH_3$. An exception is observed for sulfur, where the charge on the S atom is significantly smaller and comparable to that of hydrogen atoms.

On the other hand, the specific type of interaction between all adsorbed molecules and gold surfaces was thoroughly analyzed by calculating the projected density of states (PDOS) for each system. Our investigation focused exclusively on the 5d orbitals of the gold atoms in direct interaction with the organic molecule and the p orbitals of the chalcogen atoms (X = S, Se, Te) from the adsorbed molecules (XH_2, $XHCH_3$, XHC_6H_{11}). For comparison, we examined these interactions on both the specific most and least stable gold surface orientations for each system.

Across all investigated systems and surface orientations, the PDOS of the chalcogen p orbitals consistently show contributions within the energy range of the gold 5d states, indicating an electronic interaction, most likely covalent in nature. A clear trend emerges with respect to the chalcogen identity: as we move from S (green lines in the PDOS) to Se (red lines) and then to Te (blue lines), the contribution of the p orbitals in the energy region above the Fermi level is systematically shifted to lower energies. This trend is exemplified in Fig. 7 for the $AuXH_2$

systems and further corroborated by the $AuXHCH_3$ and $AuXHC_6H_{11}$ systems presented in Fig. S5 and S6, respectively. For tellurium, these p-orbital contributions even overlap significantly with E_f. This shift of chalcogen p-orbital density to energies below E_f enhances the covalent bond character between the metallic surface and the chalcogen atom. This progressive strengthening of the covalent Au–X interaction can be attributed to the increasing atomic size and polarizability of the heavier chalcogens, which lead to more diffuse p-orbitals capable of more extensive orbital overlap with the gold 5d-orbitals.

Comparing the most stable (represented by plain lines) and least stable (represented by dotted lines) gold surfaces further elucidates the adsorption mechanism. While the fundamental Au–X bond character is present on both, the PDOS of the more stable surfaces often exhibits subtly enhanced or broader features related to orbital interaction compared to the less stable surface. Notably, on the most stable surfaces, the

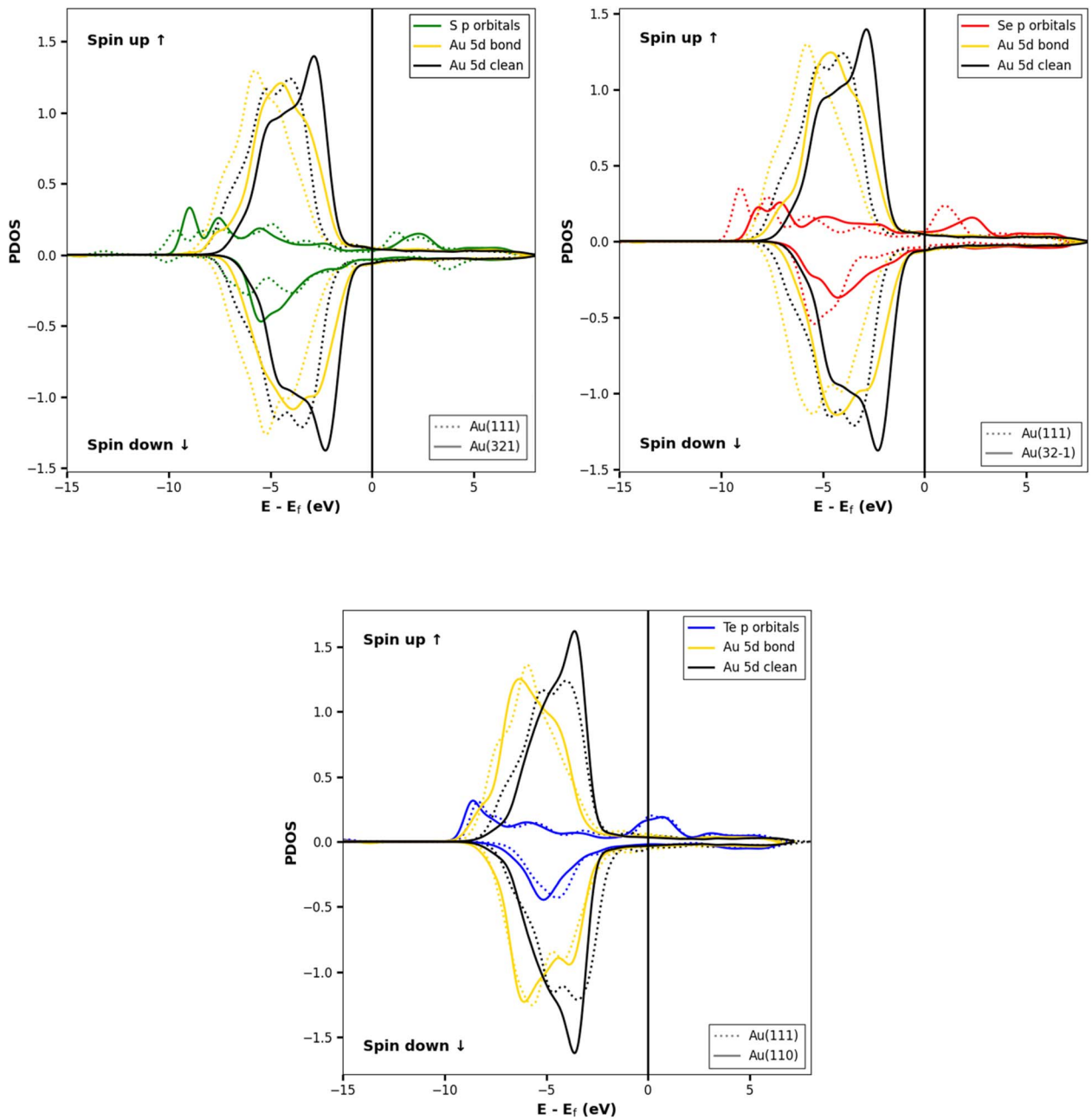

Fig. 7 Spin-polarized projected density of states (PDOS) for systems $AuXH_2$ with chalcogen (X = S, Se, Te) p-orbitals and gold 5d-orbitals on clean and adsorbed surfaces. Chalcogen p-orbitals are shown with distinct colors (green for S, red for Se, blue for Te), while Au 5d "bond" orbitals (gold) are for the adsorbed system and Au 5d "clean" orbitals (black) are for the clean slab. Plots include the least and most stable surface termination for each system: dotted lines represent the least stable, and solid lines represent the most stable. All PDOS are aligned to their respective Fermi energies (E_f).

chalcogen p orbitals are observed to shift to higher energies, which in turn increases the potential for overlapping with the 5d orbitals of the gold atoms. The electronic structure of the clean gold surfaces (represented by black lines) also plays a crucial role. For all systems, we observe either a shift or a broadening of the gold 5d orbital PDOS across the energy range upon adsorption, compared to the clean surface. This directly reflects the electronic rearrangement and charge redistribution associated with the bond formation at the interface.

Beyond the chalcogen atom, the molecular ligands (H_2, CH_3, and XHC_6H_{11}, typically ordered from top to bottom in the figures for a given chalcogen) introduce subtle modulations to the overall electronic structure. Although the core Au–X interaction dominates, the presence of electron-donating groups like CH_3 and the bulkier cyclohexyl can influence the local electron density around the chalcogen and indirectly affect the orbital interactions. These ligands induce minor alterations in the peak shapes and intensities of both the chalcogen p-orbitals and the interacting gold d-orbitals in the PDOS. For instance, the CH_3 group often leads to an intensity of the PDOS that is approximately twice as high as that observed for the H_2 or cyclohexyl groups, suggesting a more significant contribution to the density of states from this ligand.

5. Conclusion

This theoretical study elucidates the interplay between chalcogen identity, substituent size, and surface morphology in determining the adsorption strength and geometry of Au(XR) systems on gold surfaces. Three key trends emerge. Chalcogen effect: The interaction strength follows the order Te > Se > S, consistent with increasing polarizability and enhanced charge transfer from the surface to the ligand. Substituent effect: bulkier groups ($-C_6H_{11}$) amplify adsorption energies through larger dispersion contributions and greater surface contact. Surface effect: compact surfaces like Au(111) favor dispersion dominated, vertical adsorption, while stepped or chiral facets Au(110), Au(321), Au($32\bar{1}$) promote chemisorbed bridge configurations with shorter X–Au distances.

Electronic-structure analysis through PDOS further supports these trends, revealing systematic strengthening of the Au–X covalent interaction from S → Se → Te, accompanied by increased p(X)–d(Au) hybridization and characteristic shifts of chalcogen p-states toward the Fermi level. These features are more pronounced on the most stable adsorption orientations, confirming that geometric stabilization and electronic rehybridization act cooperatively to define the adsorption mechanism.

A key finding is the identification of a dispersion contribution threshold (~45%), beyond which the adsorption mechanism shifts from physisorption to chemisorption. This provides a quantitative descriptor for predicting adsorption modes across different surfaces. Overall, the results underscore the necessity of including dispersion corrections in DFT simulations to accurately capture adsorption energies and geometries, particularly for systems involving heavy chalcogens and bulky ligands. The combined energetic and electronic insights presented here establish a coherent framework for understanding and designing gold–chalcogen interfaces, opening avenues in catalysis, self-assembled nanostructures, and molecular electronics.

Conflicts of interest

The authors declare that they have no known competing financial interests or personal relationships that could have appeared to influence the work reported in this paper.

Data availability

The provided dataset comprises all relevant computational files, including initial and optimized geometries (CONTCAR) and input parameters (INCAR, KPOINTS), alongside the data used to generate the figures and tables. In compliance with the VASP license, POTCAR files are not included; however, the specific VASP version, PAW pseudopotentials used, and file hashes for verification are detailed in the README for full reproducibility.

Supplementary information (SI): additional figures, tables, computational details, adsorption geometries, PDOS analyses, and supplementary calculations that complement the discussion in the main manuscript. See DOI: https://doi.org/10.1039/d5ra08118a.

Acknowledgements

International Research project of Universidad Finis Terrae (CICI-2023) and financial support of this work under Fondecyt project 1220087 are gratefully appreciated. This research was partially supported by the supercomputing infrastructure of the NLHPC (CCSS210001). This project was provided with computing HPC and storage resources by GENCI at IDRIS thanks to the grant 2025-802131 on the supercomputer Jean Zay CSL/V100 partition.

References

1 B. Kang, M. A. Mackey and M. A. El-Sayed, Nuclear targeting of gold nanoparticles in cancer cells induces DNA damage, causing cytokinesis arrest and apoptosis, *J. Am. Chem. Soc.*, 2010, **132**, 1517–1519, DOI: 10.1021/ja9102698.

2 S. Lee, A. Puck, M. Graupe, R. Colorado, Y.-S. Shon, T. R. Lee and S. S. Perry, Structure, Wettability, and Frictional Properties of Phenyl-Terminated Self-Assembled Monolayers on Gold, *Langmuir*, 2001, **17**, 7364–7370, DOI: 10.1021/la0111497.

3 J. E. Houston and H. I. Kim, Adhesion, Friction, and Mechanical Properties of Functionalized Alkanethiol Self-Assembled Monolayers, *Acc. Chem. Res.*, 2002, **35**, 547–553, DOI: 10.1021/ar9801144.

4 J. Jia, A. Kara, L. Pasquali, A. Bendounan, F. Sirotti and V. A. Esaulov, On sulfur core level binding energies in thiol self-assembly and alternative adsorption sites: An

experimental and theoretical study, *J. Chem. Phys.*, 2015, **143**, 104702, DOI: 10.1063/1.4929350.

5 M. Haruta, When gold is not noble: catalysis by nanoparticles, *Chem. Rec.*, 2003, **3**, 75–87, DOI: 10.1002/tcr.10053.

6 M. C. Daniel and D. Astruc, Gold Nanoparticles: Assembly, Supramolecular Chemistry, Quantum-Size-Related Properties, and Applications toward Biology, Catalysis, and Nanotechnology, *Chem. Rev.*, 2004, **104**, 293–346, DOI: 10.1021/cr030698+.

7 A. S. K. Hashmi and G. J. Hutchings, Gold Catalysis, *Angew. Chem., Int. Ed.*, 2006, **45**, 7896–7936, DOI: 10.1002/anie.200602454.

8 D. T. Thompson, Using gold nanoparticles for catalysis, *Nano Today*, 2007, **2**, 40–43, DOI: 10.1016/S1748-0132(07)70116-0.

9 L. Pasquato, P. Pengo and P. J. Scrimin, Functional gold nanoparticles for recognition and catalysis, *Mater. Chem.*, 2004, **14**, 3481–3487, DOI: 10.1039/B410476E.

10 N. Khalfaoui-Hassani, M. Tabut, N. H. Awe, C. Desmarets, D. Toffoli, M. Stener, N. Goubet, M. Calatayud and C. Salzemann, The intriguing role of l-cysteine in the modulation of chiroplasmonic properties of chiral gold nano-arrows, *Nanoscale*, 2025, **17**(7), 3973–3982, DOI: 10.1039/D4NR04131C.

11 B. Ni, M. Mychinko, S. Gómez-Graña, J. Morales-Vidal, M. Obelleiro-Liz, W. Heyvaert, D. Vila-Liarte, X. Zhuo, W. Albrecht, M. Zheng, G. González-Rubio, J. M. Taboada, F. Obelleiro, N. López, J. Pérez-Juste, I. Pastoriza-Santos, H. Cölfen, S. Bals and L. M. Liz-Marzán, Chiral Seeded Growth of Gold Nanorods Into Fourfold Twisted Nanoparticles with Plasmonic Optical Activity, *Adv. Mater.*, 2023, **35**, 2208299, DOI: 10.1002/adma.202208299.

12 J. C. Love, L. A. Estroff, J. K. Kriebel, R. G. Nuzzo and G. M. Whitesides, Self-Assembled Monolayers of Thiolates on Metals as a Form of Nanotechnology, *Chem. Rev.*, 2005, **105**, 1103–1170, DOI: 10.1021/cr0300789.

13 L. Newton, T. Slater, N. Clark and A. Vijayaraghavan, Self assembled monolayers (SAMs) on metallic surfaces (gold and graphene) for electronic applications, *J. Mater. Chem. C*, 2013, **1**, 376–393, DOI: 10.1039/C2TC00146B.

14 M. S. Inkpen, Z. Liu, H. Li, L. M. Campos, J. B. Neaton and L. Venkataraman, Non-chemisorbed gold–sulfur binding prevails in self-assembled monolayers, *Nat. Chem.*, 2019, **11**, 351–358, DOI: 10.1038/s41557-019-0216-y.

15 M. Dolci, D. Toulemon, Z. Chaffar, J.-L. Bubendorff, F. Tielens, M. Calatayud, S. Zafeiratos, S. Begin-Colin and B. P. Pichon, Nanoparticle Assembling through Click Chemistry Directed by Mixed SAMs for Magnetic Applications, *ACS Appl. Nano Mater.*, 2019, **2**(1), 554–565, DOI: 10.1021/acsanm.8b02152.

16 R. A. Boto, J. Contreras-García and M. Calatayud, The role of dispersion forces in metal-supported self-assembled monolayers, *Comput. Theor. Chem.*, 2015, **1053**, 322–327.

17 A. Li, J.-P. Piquemal, J. Richardi and M. Calatayud, Butanethiol adsorption and dissociation on Ag (111): A periodic DFT study, *Surf. Sci.*, 2016, **646**, 247–252, DOI: 10.1016/j.susc.2015.06.009.

18 C. L. McGuiness, G. A. Diehl, D. Blasini, D.-M. Smilgies, M. Zhu, N. Samarth, T. Weidner, N. Ballav, M. Zharnikov and D. L. Allara, Molecular Self-Assembly at Bare Semiconductor Surfaces: Cooperative Substrate−Molecule Effects in Octadecanethiolate Monolayer Assemblies on GaAs(111), (110), and (100), *ACS Nano*, 2010, **4**, 3447–3465, DOI: 10.1021/nn1004638.

19 H. J. Lee, A. C. Jamison and T. R. Lee, Surface Dipoles: A Growing Body of Evidence Supports Their Impact and Importance, *Acc. Chem. Res.*, 2015, **48**, 3007–3015, DOI: 10.1021/acs.accounts.5b00307.

20 R. Sardar, A. M. Funston, P. Mulvaney and R. W. Murray, Gold Nanoparticles: Past, Present, and Future, *Langmuir*, 2009, **25**, 13840–13851, DOI: 10.1021/la9019475.

21 N. Mameka, L. Lührs, S. Heissler, H. Gliemann and C. Wöll, Tailoring the Strength of Nanoporous Gold by Self-Assembled Monolayers of Alkanethiols, *ACS Appl. Nano Mater.*, 2018, **1**, 6613–6621, DOI: 10.1021/acsanm.8b01368.

22 C. Vericat, M. E. Vela, G. Benitez, P. Carro and R. C. Salvarezza, Self-assembled monolayers of thiols and dithiols on gold: new challenges for a well-known system, *Chem. Soc. Rev.*, 2010, **39**, 1805–1834, DOI: 10.1039/B907301A.

23 E. Pensa, E. Cortés, G. Corthey, P. Carro, C. Vericat, M. H. Fonticelli, G. Benítez, A. A. Rubert and R. C. Salvarezza, The chemistry of the sulfur-gold interface: in search of a unified model, *Acc. Chem. Res.*, 2012, **45**, 1183–1192, DOI: 10.1021/ar200260p.

24 H. Häkkinen, The gold–sulfur interface at the nanoscale, *Nat. Chem.*, 2012, **4**, 443–455, DOI: 10.1038/nchem.1352.

25 O. Zenasni, M. D. Marquez, A. C. Jamison, H. J. Lee, A. Czader and T. R. Lee, Inverted Surface Dipoles in Fluorinated Self-Assembled Monolayers, *Chem. Mater.*, 2015, **27**, 7433–7446, DOI: 10.1021/acs.chemmater.5b03411.

26 H. Chen, C. K. Heng, P. D. Puiu, X. D. Zhou, A. C. Lee, T. M. Lim and S. N. Tan, Detection of Saccharomyces cerevisiae immobilized on self-assembled monolayer (SAM) of alkanethiolate using electrochemical impedance spectroscopy, *Anal. Chim. Acta*, 2005, **554**, 52–59, DOI: 10.1016/j.aca.2005.08.086.

27 S. Li, Q. Luo, Z. Zhang, G. Shen, H. Wu, A. Chen, X. Liu, M. Li and A. Zhang, Electrochemistry Study of Permselectivity and Interfacial Electron Transfers of a Branch-Tailed Fluorosurfactant Self-Assembled Monolayer on Gold, *Molecules*, 2018, **23**(11), 2998, DOI: 10.3390/molecules23112998.

28 F. Tielens, V. Humblot, C.-M. Pradier, M. Calatayud and F. Illas, Stability of Binary SAMs Formed by ω-Acid and Alcohol Functionalized Thiol Mixtures, *Langmuir*, 2009, **25**(17), 9980–9985, DOI: 10.1021/la901127g.

29 J. R. Reimers, M. J. Ford, S. M. Marcuccio, J. Ulstrup and N. S. Hush, Competition of van der Waals and chemical forces on gold–sulfur surfaces and nanoparticles, *Nat. Rev. Chem.*, 2017, **1**, 17, DOI: 10.1038/s41570-0017.

30 S. Miranda-Rojas and F. Mendizabal, Exploration of the Interaction Strength at the Interface of Anionic Chalcogen Anchors and Gold (111)-Based Nanomaterials, *Nanomaterials*, 2020, **10**, 1237, DOI: 10.3390/nano10061237.
31 D. J. Liu, J. W. Evans, P. M. Spurgeon and P. A. Thiel, Structure of chalcogen overlayers on Au(111): Density functional theory and lattice-gas modeling, *J. Chem. Phys.*, 2020, **152**(22), 224706, DOI: 10.1063/5.0006131.
32 K. Schouteden, J. Debehets, D. Muzychenko, Z. Li, J. W. Seo and C. Van Haesendonck, Adsorption of Te atoms on Au(111) and the emergence of an adatom-induced bound state, *J. Phys. Condens. Matter.*, 2017, **29**, 12, DOI: 10.1088/1361-648X/aa5b82.
33 J. Morales-Vidal, N. López and M. A. Ortuño, Chirality Transfer in Gold Nanoparticles by l-Cysteine Amino Acid: A First-Principles Study, *J. Phys. Chem. C*, 2019, **123**(22), 13758–13764, DOI: 10.1021/acs.jpcc.9b02918.
34 J. P. Perdew, K. Burke and M. Ernzerhof, Generalized Gradient Approximation Made Simple, *Phys. Rev. Lett.*, 1996, **77**, 3865–3868, DOI: 10.1103/PhysRevLett.77.3865.
35 M. Rosa, S. Corni and R. Di Felice, Van der Waals Effects at Molecule–Metal Interfaces, *Phys. Rev. B*, 2014, **90**, 125448, DOI: 10.1103/PhysRevB.90.125448.
36 S. Grimme, J. Antony, S. Ehrlich and H. Krieg, A Consistent and Accurate Ab Initio Parametrization of Density Functional Dispersion Correction (DFT-D) for the 94 Elements H-Pu, *J. Chem. Phys.*, 2010, **132**, 154104, DOI: 10.1063/1.3382344.
37 G. Kresse and J. Hafner, Ab initio molecular dynamics for liquid metals, *Phys. Rev. B*, 1994, **47**, 558, DOI: 10.1103/PhysRevB.47.558.
38 G. Kresse and J. Furthmaller, Efficiency of Ab-Initio Total Energy Calculations for Metals and Semiconductors Using a Plane-Wave Basis Set, *Comput. Mater. Sci.*, 1996, **6**, 15, DOI: 10.1016/0927-0256(96)00008-0.
39 G. Kresse and J. Furthmaller, Efficient iterative schemes for ab initio total-energy calculations using a plane-wave basis set, *Phys. Rev. B*, 1996, **54**, 11–169, DOI: 10.1103/physrevb.54.11169.
40 G. Kresse and J. Hafner, Norm-conserving and ultrasoft pseudopotentials for first-row and transition elements, *J. Phys.: Condens. Matter*, 1994, **6**, 8245, DOI: 10.1088/0953-8984/6/40/015.
41 G. Kresse and D. Joubert, From Ultrasoft Pseudopotentials to the Projector Augmented-Wave Method, *Phys. Rev. B: Condens. Matter Mater. Phys.*, 1999, **59**, 1758–1775, DOI: 10.1103/PhysRevB.59.1758.
42 M. Tabut, P. V. Stishenko and M. Calatayud, Modeling the self-assembly of L-cysteine molecules on the Au(111) surface: A lattice model approach, *Surf. Sci.*, 2025, **757**, 122740, DOI: 10.1016/j.susc.2025.122740.
43 Q. Li, M. Rellán-Piñeiro, N. Almora-Barrios, M. Garcia-Ratés, I. N. Remediakis and N. López, Shape Control in Concave Metal Nanoparticles by Etching, *Nanoscale*, 2017, **9**, 13089–13094, DOI: 10.1039/C7NR03889E.
44 G. Makov and M. C. Payne, Periodic Boundary Conditions in Ab Initio Calculations, *Phys. Rev. B: Condens. Matter Mater. Phys.*, 1995, **51**, 4014–4022, DOI: 10.1103/PhysRevB.51.4014.
45 H. J. Monkhorst and J. D. Pack, Special Points for Brillouin-zone Integrations, *Phys. Rev. B*, 1976, **13**, 5188–5192, DOI: 10.1103/PhysRevB.13.5188.
46 K. Momma and F. Izumi, VESTA 3 for Three-Dimensional Visualization of Crystal, Volumetric and Morphology Data, *J. Appl. Crystallogr.*, 2011, **44**, 1272–1276, DOI: 10.1107/S0021889811038970.
47 C. F. McFadden, P. S. Cremer and A. J. Gellman, Adsorption of Chiral Alcohols on "Chiral" Metal Surfaces, *Langmuir*, 1996, **12**, 2483–2487, DOI: 10.1021/la950348l.
48 M. Calatayud, J. Andrés and A. Beltrán, A theoretical analysis of adsorption and dissociation of CH3OH on the stoichiometric SnO2(110) surface, *Surf. Sci.*, 1999, **430**(1–3), 213–222, DOI: 10.1016/s0039-6028(99)00507-5.
49 L. Vitos, A. V. Ruban, H. L. Skriver and J. Kollár, The surface energy of metals, *Surf. Sci.*, 1998, **411**(1–2), 186–202, DOI: 10.1016/s0039-6028(98)00363-x.
50 I. Galanakis, N. Papanikolaou and P. H. Dederichs, Applicability of the broken-bond rule to the surface energy of the fcc metals, *Surf. Sci.*, 2002, **511**(1–3), 1–12, DOI: 10.1016/s0039-6028(02)01547-9.
51 D. Holec, P. Dumitraschkewitz, D. Vollath and F. D. Fischer, Surface Energy of Au Nanoparticles Depending on Their Size and Shape, *Nanomaterials*, 2020, **10**(3), 484, DOI: 10.3390/nano10030484.
52 W. R. Tyson and W. A. Miller, Surface Free Energies of Solid Metals Estimation from Liquid Surface Tension Measurements, *Surf. Sci.*, 1977, **62**, 267–276, DOI: 10.1016/0039-6028(77)90442-3.
53 D. Holec, P. Dumitraschkewitz, D. Vollath and F. D. Fischer, Surface Energy of Au Nanoparticles Depending on Their Size and Shape, *Nanomaterials*, 2020, **10**(3), 484, DOI: 10.3390/nano10030484.
54 J. Ning, M. Kothakonda, J. W. Furness, A. D. Kaplan, S. Ehlert, J. G. Brandenburg, J. P. Perdew and J. Sun, Workhorse minimally empirical dispersion-corrected density functional with tests for weakly bound systems: r^2SCAN+rVV10, *Phys. Rev. B*, 2022, **106**(7), 075422, DOI: 10.1103/PhysRevB.106.075422.
55 F. L. Maza, P. Carro, C. Vericat, K. Kern, R. C. Salvarezza and D. Grumelli, Role of Gold Adatoms in the Adsorption of Sulfide Species on the Gold(001)-hex Surface, *J. Phys. Chem. C*, 2018, **122**(4), 2207–2214, DOI: 10.1021/acs.jpcc.7b11059.
56 R. L. McCarley, Y. T. Kim and A. J. Bard, Scanning tunneling microscopy and quartz crystal microbalance studies of gold exposed to sulfide, thiocyanate, and n-octadecanethiol, *J. Phys. Chem.*, 1993, **97**(1), 211–215, DOI: 10.1021/j100103a036.
57 X. m. Guo and G. X. Wei, Determination of ultra-trace amounts of selenium by continuous flow hydride generation AFS and AAS with collection on gold wire, *J. Anal. At. Spectrom.*, 2001, **16**(12), 1414–1418, DOI: 10.1039/b105737p.

58 S. Miranda-Rojas, R. Salazar-Molina, J. Kästner, R. Arratia-Pérez and F. Mendizábal, Theoretical exploration of seleno and tellurophenols as promising alternatives to sulfur ligands for anchoring to gold (111) materials, *RSC Adv.*, 2016, **6**(6), 4458–4468, DOI: 10.1039/C5RA21964G.

59 S. Miranda-Rojas, A. Muñoz-Castro, R. Arratia-Perez and F. Mendizabal, Theoretical insights into the adsorption of neutral, radical and anionic thiophenols on gold(111), *Phys. Chem. Chem. Phys.*, 2013, **15**, 20363, DOI: 10.1039/C3CP53591F.

60 F. P. Cometto, P. Paredes-Olivera, V. A. Macagno and E. M. Patrito, Density Functional Theory Study of the Adsorption of Alkanethiols on Cu(111), Ag(111), and Au(111) in the Low and High Coverage Regimes, *J. Phys. Chem. B*, 2005, **109**(46), 21737–21748, DOI: 10.1021/jp053273v.